DOPING EFFECTS ON ORGANIC INTERFACES

A Thesis
by
CORTNEY BOUGHER

Submitted to the Graduate School
at Appalachian State University
in partial fulfillment of the requirements for the degree of
MASTER OF SCIENCE

May 2014
Department of Physics and Astronomy

DOPING EFFECTS ON ORGANIC INTERFACES

A Thesis
by
CORTNEY BOUGHER
May 2014

APPROVED BY:

Brad R. Conrad
Chairperson, Thesis Committee

Tonya S. Coffey
Member, Thesis Committee

Oana D. Jurchescu
Member, Thesis Committee

Michael Briley
Chairperson, Department of Physics and Astronomy

Edelma D. Huntley
Dean, Cratis Williams Graduate School

Abstract

DOPING EFFECTS ON ORGANIC INTERFACES

Cortney Bougher
B.S., Appalachian State University
M.S., Appalachian State University

Chairperson: Brad R. Conrad

Organic semiconductors are an important technology currently being used in applications such as organic LED displays, flexible solar cell panels, transparent transistors, and other low-cost electronics. Organic electronics are an integral area of research because these organic semiconductors can be lightweight, flexible, and biodegradable with low-cost production methods such as ink-jet or roll-to-roll printing. These inexpensive mass production techniques require solution deposition of the organic material. While single crystal organic semiconductors have been shown to exhibit carrier mobilities comparable to the silicon currently used in photovoltaics, during solution deposition of common organic semiconducting materials the resultant thin film is often polycrystalline. Device performance and electrical properties of organic thin-film transistors are highly dependent on crystal structure and molecular packing. In polycrystalline thin films, boundary regions between crystal grains can affect the overall performance of devices, as crystal structure and packing may differ from that of the surrounding crystal regions. These boundary regions may also serve

as defect sites, allowing environmental factors, such as oxygen content and humidity, to alter local charge transport through devices. We utilize Kelvin Probe Force Microscopy (KPFM), a mode of tapping Atomic Force Microscopy (AFM), to characterize how grain boundaries alter local conductivity and device performance as a function of doping in 2,8-difluoro-5,11-triethysilylethynyl anthradithiophene (diF TESADT) thin-film transistor surfaces. Device voltage drops at grain boundaries are characterized as a function of both atmospheric dopants and transition time between dopants.

Acknowledgments

From the moment I walked into Brad's office at the beginning of my junior year, he had me excited about science and research. I owe thanks to his drive, determination, and passion as a scientist; it is those qualities which have inspired me along this journey; however, it has been Brad's patience and understanding that have guided me through the most difficult parts of this process. I would not be the scientist or person that I am today without Brad, my thesis advisor, mentor, and friend.

Thank you to everyone who has worked in our research lab, those who have helped change pump oil, those who have made coffee, and those who have watched the AFM so that I might retain some sanity; particularly Eitan Lees and Andrew Zeidell. Thank you especially to Shawn Huston, for all the help in getting this project going, through all the stops and starts.

Thank you to my thesis committee, Tonya Coffey and Oana Jurchescu. Tonya has taught me so much about writing and microscopy and Oana has been a wonderful collaborator and teacher.

I would like to thank the Physics and Astronomy department at Appalachian State University. This has been my home for six years; I have learned and grown more than I ever hoped in that time. In particular, I want to thank Angela Owen. She has answered every question, checked every form, fixed every problem, and generally brightened every day.

I gratefully acknowledge funding from the North Carolina Space Grant Consortium and the Appalachian State University Office of Student Research. Without these excellent resources this work would not have been possible.

Dedication

To Joshua, my hope and my future

Table of Contents

Forward

This work will be submitted to *Applied Physical Letters*, an international peer-reviewed journal published by the *American Institute of Physics*; it has been formatted according to the style guide for *American Institute of Physics* journals.

INTRODUCTION

Organic semiconductors are an important, developing technology that can be used in making flexible solar cells, organic LED displays, simple transistor switches, and low-cost electronics[1,2]. While organic LEDs are the most commercially successful class of the organic electronics to date, the development of low-cost organic circuitry has made major advances within the last decade. Examples of these advances include an organic, flexible, non-volatile, 64-bit memory cell[3], a flexible, ultrathin solar cell which is semi-transparent and has high internal efficiencies[4], and ultra-high mobility transparent organic transistors, with reported electronic mobilities as large as 43 cm^2/Vs [5]. Advances such as these highlight the potential of organic materials to change and improve the ways technology is used. The potential for low-cost fabrication on a variety of non-traditional surfaces could allow for seamless technology on a vast scale[6]. Recently, advances in high-performance organic semiconductors that are designed to be solution processable have allowed this vision to be more clearly realized. Through the optimization of the materials to be used in solution deposition fabrication techniques, the dream of large-scale device fabrication on arbitrary surfaces can be fully realized.

From a purely theoretical point of view, physical vapor deposition is the easiest deposition method to model and cleanest system to design. Unfortunately, devices produced using this method are expensive and have shown a large variance in morphological structure and electrical behavior[7,8]. In sharp contrast, deposition through doctor blading, ink-jet, and

printing press style deposition onto flexible substrates such as plastic and paper can be extremely fast and an efficient use of potentially expensive materials[9–13]. Furthermore, these methods are often used in the mass production of printed materials. Since these high-efficiency methods primarily use solution deposition, analogous laboratory scale fabrication methods such as spin-coating, ink-jet, and drop casting are commonly used to simulate the large scale methods. While inherently a more complicated deposition method, thin films deposited by solution are the most technically relevant and must be studied if the relative cost per device is to be decreased. Specifically, solution deposited organic thin films display a unique set of morphological and electrical characteristics are an area of intense research within the field, and a focus of this thesis.

There are several mechanisms which limit device performance in thin-film organic electronic devices; a schematic of an organic thin-film transistor is given in Fig. 1. Charge transport from the metal electrode into the organic semiconductor has been a long standing problem within the field[14,15]. The interaction of the semiconductor and gate dielectric for FET

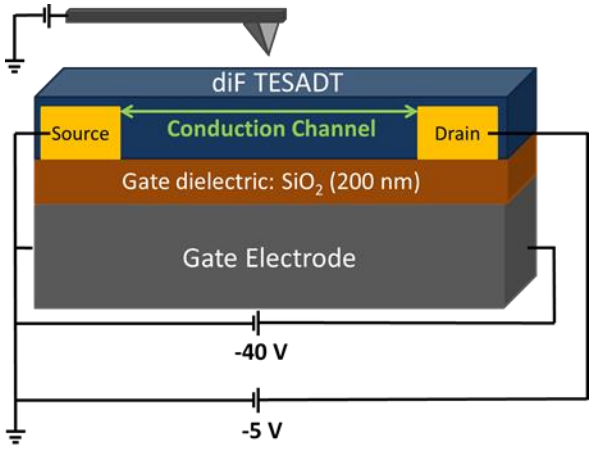

FIG 1. TFT device geometry: p-doped electrode (grey), thermally grown SiO_2 gate dielectric (brown), AU/Ti source and drain contacts (yellow), and diF TESADT thin-film organic semiconductor (blue).

devices can also limit charge carrier densities and therefore device performance.[16] For thin-film transistors the conduction of charge carriers in the first few molecular layers normal to the conduction channel of the device determines the bulk electronic properties of the film[17–19]; however, one of the largest problems associated with thin-film growth of organic electronics is the bulk film morphology and the ability to control material crystallization. Polycrystalline films that display transport characteristics that vary with local crystallization, specifically the conduction between grains, and relative crystal orientation has been a point of much study.[20] Since ideally these devices are to be used in ambient conditions and complex environments, possible doping of the film grain boundaries and even the bulk thin-film material has been of particular interest.[21,22] It has been shown that doping increases with the presence of grains and grain boundaries, in comparison to solely local bulk crystal interfaces[22,23]. While both chemical and gas doping is relevant to organic thin-film transistor development, atmospheric doping provides a unique system to study for devices to be used in the most likely common set of conditions.

It is well known that the electrical performances of both organic and inorganic transistors are highly dependent on the crystal structure of the bulk organic material[24–26]. Goetz and colleagues demonstrate this dependence, as well as the relationship between chemical structure and bulk crystal structure, in a study of commercially relevant anthradithiophene derivatives[25]. The molecule difluoro tri-*sec*-butylsilylethynyl anthradithiophene (F-TSBS-ADT) has three benzene rings in a linear chain backbone structure, as shown in Fig. 2. Using F-TSBS-ADT as a point for comparison, the backbone length was increased to four benzene rings in F-TSBS tetracenedithiophene (F-TSBS-TDT), and to five benzene rings for F-TSBS pentacenedithiophene (F-TSBS-PDT). While different

only in the length of the backbone structure, these three molecules yield devices with very different crystal structure and electrical properties. Goetz determined that crystalline order and intermolecule π-stacking were increased with increased backbone length, and that this

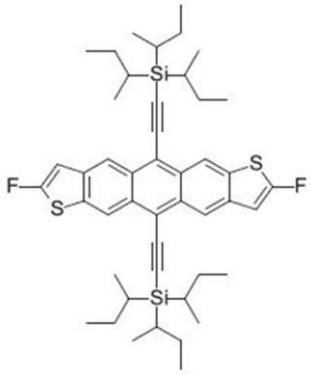

FIG 2. Chemical structure F TSBS ADT

directly correlated with enhance electrical performance. The electrical mobility of F-TSBS-PDT is three orders of magnitude larger than that of F-TSBS-ADT. Goetz and many others[27–29] show that altering the chemical structure of organic molecules greatly impacts morphology, and therefore electrical performance. Once high performance organic semiconductors have been identified, optimization of growth modes and device fabrication techniques is required. Another method of modifying film growth and morphology is through chemical modification of the growth surfaces, specifically the electrodes.

Such surface treatments are often used in organic transistor device fabrication because such treatments increase π-π overlap of semiconductor molecules and crystalline order in bulk films[30,31]. Grazing incidence X-ray diffraction shows that, with perfluorinated benzene thiol used as a Au drain and source contact surface treatment, diF-TESADT forms a crystal structure in the (001) mode.[31,32] The diF-TESADT (001) crystal orientation is preferential in this case because the π-plane is perpendicular to the surface, enabling charge transport parallel to the surface through the conduction channel. On untreated Au contacts

and dielectric material diF-TESADT forms crystals in the (111) mode. In this mode the molecules are perpendicular to the surface and charge transport through the conduction channel is inhibited. Kline reports that diF-TESADT TFTs with untreated contacts exhibit 10 times lower mobilities than those with PFBT treated contacts, for channel lengths 5 to 50 μm.[32] The work presented here utilizes 25 μm channel length diF TESADT solution processed devices. As such, PFBT treatments are thus used to improve crystallinity at the Au contacts and improve device mobility.

Additional work on PFBT self-assembled monolayers (SAMs) has shown improvement in diF TESADT crystallinity for Au contact TFT devices.[25,31,32] The interaction between PFBT and diF TESADT was examined by Ward and colleagues by using monofluorinated SAMs to investigate the role of the position of the halogen F on the PFBT molecule in device structure and on electronic performance.[33] The F-F interaction is proposed to be the primary driver of crystal orientation relative to the surface of the diF TESADT molecule on the Au surface.[33,34] Untreated, 2-, and 3-MFBT treated contacts all yield a mixture of the preferable (001) and undesired (111) molecular orientations; however, the 4-MFBT and PFBT treated contacts exhibit only the (001) orientation and yield significantly higher mobilities than those treatments which produce a mixture of orientations, corroborating the idea that π-π overlap is a strong predictor of electronic performance of organic semiconductors. Ward and coworkers suggest that the F-F interaction at the 4 position on the thiol benzene ring in PFBT, as discussed by Huston and colleagues[34], is the dominant interaction between the organic semiconductor molecule and the SAM treatment. It is important to note that this position on the molecule backbone also provides the strongest F-F intermolecular interaction. Thus it can be stated that the interaction between PFBT and diF

TESADT is shown to yield devices with favorable crystalline structure and higher mobilities when compared to that of other MFBT treated or untreated devices.

Because of the limited lateral growth from the electrodes reported by Gundlach[31], the bridging of the conduction channel by diF TESADT crystals for devices with channel length less than 25 μm is necessary for good charge transport through the conduction channel. This bridging effect does not, however, mean that crystal grains extend from one electrode, across the entire conduction channel, to the opposite electrode. During deposition of the diF TESADT film, crystal grains preferentially nucleate on the PFBT-treated Au contacts. These crystal grains grown across the entire contact, often growing out 10 μm from the contact onto

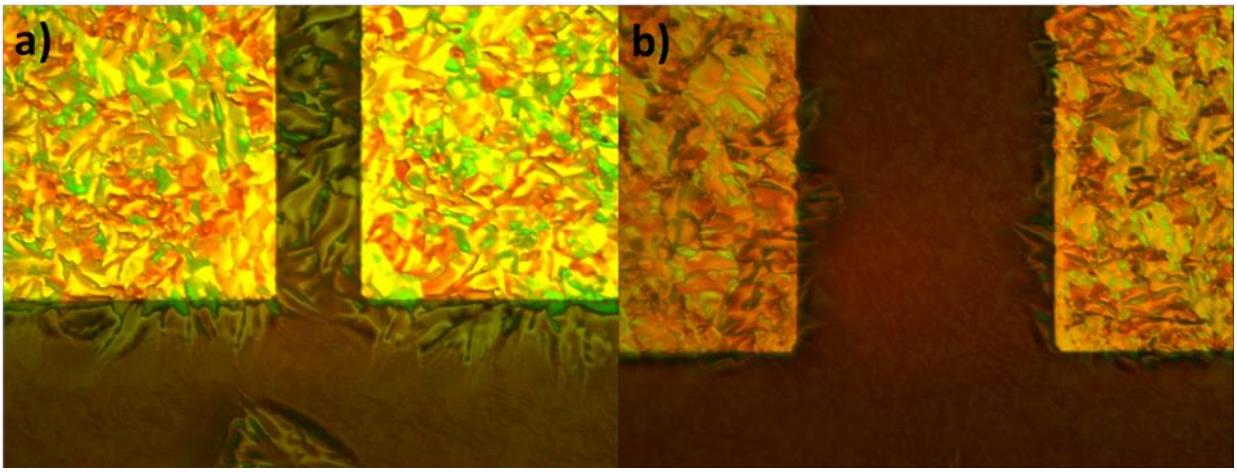

FIG 3. 50x magnified optical micrographs of the conduction channel of diF TESADT thin-film transistors where channel length L is (a) 25 μm, and (b) 75 μm.

the dielectric material. As seen in Fig. 3, crystal grains extend from each electrode into the conduction channel. For the L = 25 μm device, shown in Fig. 3a, these two fronts of grains extending from the conduction channel meet in the center of channel, yielding a large grain boundary that extends the entire width of the conduction channel. This large grain boundary is highlighted in the optical image given in Fig. 4, which is shown at 50 times magnification. The diF TESADT film is approximately 100 nm thick, and the large grain boundary is 20 nm

deep. The large grain boundary does not extend through the film to the oxide layer. As this is a distinct boundary region between the crystal structures extending from each electrode, this large grain boundary is an impediment to charge carrier mobility within the conduction channel; however, behavior at the large grain boundary is not well understood.

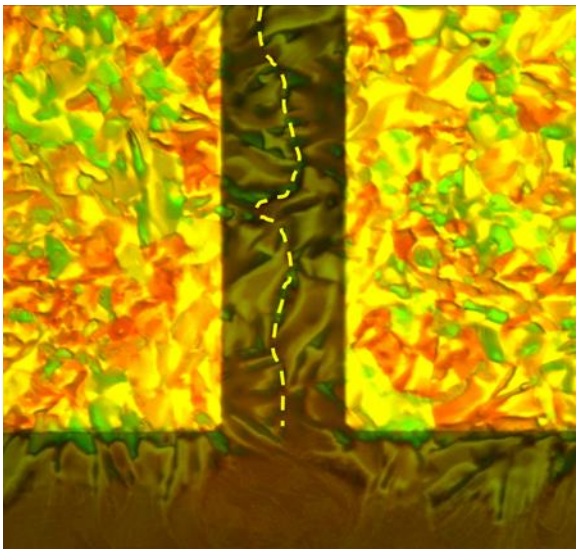

FIG 4. 50x magnified optical image of the conduction channel of a diF TESADT device in which the large grain boundary is highlighted. This grain boundary arises from crystal grains extending from the electrodes and meeting in the conduction channel.

Solution deposition of small organic molecule semiconductors, such as diF TESADT, often yields polycrystalline films, an example of which can be seen on the Au electrodes in Fig. 3. The role of grain boundaries in polycrystalline organic TFTs in relation to electron mobility degradation has been investigated.[22,35–38] One such study, performed by Weitz and colleagues, found that the degradation of an organic device was increased with a polycrystalline thin-film semiconductor[22] due to ambient gas molecules at grain boundaries. Weitz fabricated bis(1H,1Hperfluorobutyl)-dicyano-perylene tetracarboxylic diimide ($C_3F_7CH_2$-PTCDI-$(CN)_2$ TFTs using two film growth techniques, solution grown single crystals and vacuum deposition of polycrystalline films. The electron mobility of these three

devices was measured periodically over 50 000 minutes while the devices were stored in ambient air. It was observed that the electron mobility of the polycrystalline thin-film device decreased by an order of magnitude over 14 000 minutes while electron mobility of the single crystal devices stays approximately constant. This difference in the degradation of electron mobility is attributed to the high density of grain boundaries in the polycrystalline films. The disorder and reorientation of molecules at grain boundaries should allow for the inclusion of ambient gas molecules in these boundary regions much more easily than single crystal or encapsulated devices. Additional evidence is provided when Chen and coworkers studied bis(tri-isopropylsilylethynyl) (TIPS) pentacene thin films and found that mobility at the grain boundaries was about seven orders of magnitude lower than that of single crystal TIPS pentacene.[39] For other systems, including diF TES ADT, it is likely that grain boundaries significantly impact the device performance of polycrystalline devices. Polycrystalline devices should have lower electron mobilities and performance will likely degrade over time in comparison to single crystal devices.

Focusing on the electronic changes that can occur at grain boundaries, the effects of gas doping have been reported for various organic devices[22,40–43]. Jurchescu and colleagues studied how light exposure effects the process by which oxygen enhances charge carrier density in pentacene single crystals.[41] When measurements were taken in a dark environment, conductivity of the pentacene crystal went up by 25% with exposure to dry air, and conductivity went down by 45% with exposure to ambient air; however, in the same experiment when identical measurements were taken in an ambient light environment, the conductivity of the pentacene single crystal went up by 67% in dry air and by 50% in ambient air. The differences observed in the electrical properties illustrate two mechanisms,

the effects of O_2 and H_2O. Since H_2O molecules are polar, they will act as trapping sites[44] and will increase energetic disorder,[45] thus decreasing conductivity in the pentacene crystal. In addition to measuring these changes in the conductivity of the pentacene devices with exposure to dry and ambient air, Jurchescu determined that O_2 is incorporated into the crystal structure, as confirmed by thermogravimetric analysis (TGA) of a pentacene single crystal upon exposure to dry air. The electronegativity of O_2 causes an increase in the observed hole density in pentacene crystals. This increase in hole density is shown to be enhanced with exposure to ambient light, and the negative effect of H_2O is overcome[41]. Additionally, Jurchescu shows that the most significant uptake of air into the single crystal occurs within approximately 200 minutes of exposure to dry air. Thus, it is expected that molecular oxygen should increase device performance and molecular water should decrease electrical performance, but the effect of water may be limited by the greater positive effect of oxygen.

In contrast to Jurchescu's single crystal study, Ye and coworkers examined the electrical performance of pentacene TFTs under O_2 and H_2O. Upon exposure to O_2, carrier mobility was shown to increase over 300 minutes. After the first exposure to O_2, this increase in carrier mobility was also shown to be reversible under high vacuum.[42] The pentacene TFTs were also exposed to H_2O by placing them in air with a relative humidity of 80%, an increase in carrier mobility is seen over the first 120 minutes of exposure to H_2O, followed by a decrease to the initial mobility value over the following 180 minutes. Ye concludes that there are several competing effects within the device: inclusion of O_2 within the grain boundaries increases charge mobility, physically absorbed H_2O degrades device performance, and over longer exposures chemically absorbed H_2O can enhance performance

in pentacene TFTs, due to p-doping as a result of pentacene/$(H_20)_n$.[42] The inclusion of O_2 will be the focus of this work, quantification of this effect is vital if it is to be understood.

To partially probe these changes due to atmospheric doping, an important in-situ electrical characterization technique called Kelvin Probe Force Microscopy (KPFM), a tapping mode of Atomic Force Microscopy (AFM), has previously been used to qualitatively image the surface potential of diF-TESADT TFTs.[46] Teague and colleagues utilized KPFM to correlate surface potential and topographical features of diF TESADT TFTs. By correlating the surface potential and topography of a TFT conduction channel, morphological influences on electronic transport through the conduction channel were found. A 5 μm channel length diF TESADT device was imaged with KPFM; it should be noted that grain size is comparable to channel length and thus there is no large grain boundary within the device conduction channel[46], as is seen in larger channel length devices.[31,33] The KPFM potential image and corresponding AFM topographic image can be examined together, so that the behavior of surface potential may be related to topographic features as measured by AFM. When the device gate voltage is -40 V, there is a 45% voltage loss at the left electrode edge. This loss indicates that this electrode-organic interface is a significant barrier to charge transport.[46] Zaghloul and coworkers used KPFM to study charging within various components of micro- and nano-electromechanical systems.[47] They performed KPFM imaging of a charge injected SiN_x surface over time, to observe the decay of the charge in the dielectric. The same KPFM line scan is monitored through time, so that the decay of the charge injection may be observed. Following a single line scan enables observation of the evolution of that line across multiple images, while minimizing averaging effects due to pixel

size. Zaghoul shows that KPFM is a viable tool to observe systems that change in time, such as the effects of a dynamic local environment or gas intake.

While work done by other groups is insightful and important, the effect of gas doping at grain boundaries is still not well understood. Specifically, the effects of O_2, H_2O, and ambient air on high performance organic thin-film transistors with organic semiconductors with near-record mobilities for polycrystalline films, such as diF TESADT, are not well known. To this effect, several experiments have been conducted to understand the effects and mechanisms of these gas dopants and monitor their behavior as a function of time. KPFM has been utilized to image the surface potential and topography of the conduction channel of diF TESADT thin-film organic transistors in gas dopant environments.

EXPERIMENTAL SETUP AND DATA

The organic semiconductor used in this work is fluorinated 5,11-bis(triethylsilylethynyl) anthradithiophene (diF TESADT). diF TESADT is a solution-processable, p-type organic semiconductor[48], the chemical structure of diF TESADT is given in Fig. 5. The backbone structure of this molecule is an anthradithiophene,[49,50] with triethylsilylethynyl side groups for improved solubility. When solution deposited TESADT has been shown to produce an amorphous film, to improve crystallinity as well as stability

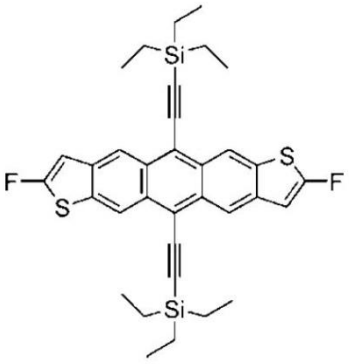

FIG 5. Chemical structure of diF TESADT

the molecule is partially fluorinated.[51] Both syn- and anti-isomers are present, this does not significantly affect the behavior of the semiconductor.[49] The molecule is synthesized as reported by Subramanian and coworkers.[51]

DiF TESADT thin-film transistor devices for this work were fabricated using the spin-coat method. Pre-manufactured SiO_2 substrates with 5 nm Ti and 45 nm Au electrode patterns were used as the base of the samples. Samples were sonicated in acetone, sonicated in isopropanol alcohol, cleaned with UV-O_3, rinsed in H_2O, and dried under N_2. The PFBT treatment was prepared by sonicating in ethanol, and applying the treatment to the substrate. The samples were then sonicated in ethanol, rinsed with acetone, and dried in N_2. The diF

TESADT was then sonicated in a chlorobenzene solvent for 5 minutes, heated at 55˚C, and spin-coat deposited onto the surface of the samples. Samples were stored in high vacuum overnight, at least 12 hours prior to any experiment. The following day optical images were taken of conduction channels of various devices, and all devices on the sample were electrically characterized in air.

In the post-fabrication characterization of the tested diF TESADT devices polarized optical images are taken. Such an optical micrograph of an entire device at 5 times

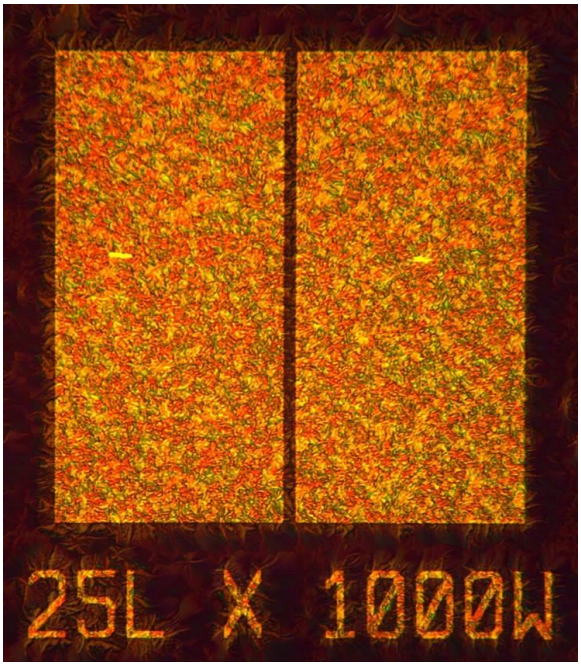

FIG 6. A polarized optical image of a single diF TESADT thin-film transistor device, device width is 1000 µm, channel length is 25 µm.

magnification is shown in Fig. 6. This image is typical of all devices utilized in this work, with conduction channel width of 1000 µm and length of 25 µm. The polarized optical image of the conduction channel of a 25 µm channel-length device is shown in Fig. 7. Large crystal grains are seen both on top of the electrodes and extending up to 10 µm outward from the

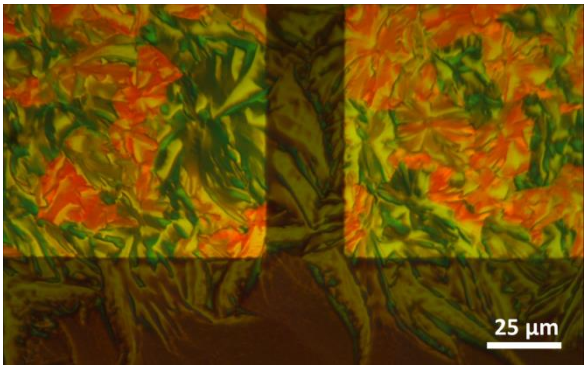

FIG 7. A polarized optical image of the conduction channel of a 25 µm channel-length device. Note the formation of large grains on the electrodes and extending outwards from both electrodes.

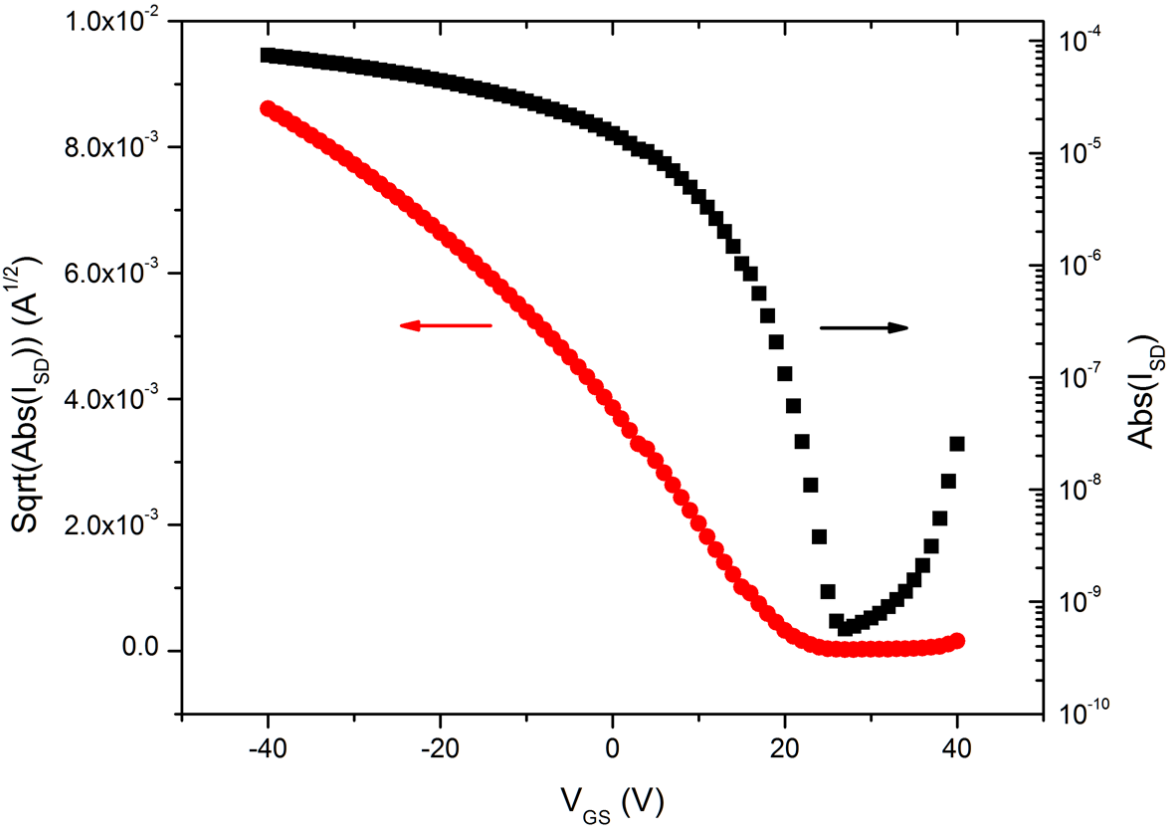

FIG 8. Current-voltage curves for a typical diF TESADT TFT device. The square root of the absolute value of the source-drain current is plotted versus the gate-drain voltage on the left axis. The absolute value of the source-drain current is plotted as a function of gate-source voltage. Typical devices have a saturation µ of 0.12 cm^2/Vs and an on/off current ratio of 10^6.

electrodes. The grains extend outward into the conduction channel of the device as described by Gundlach and coworkers[31], forming a large grain boundary through the center of the conduction channel. The device current as a function of gate-source voltage shows these

devices have an on/off current ratio of 10^6, as seen in Fig. 8 which shows the absolute current and square root of absolute current as a function of gate-source voltage. Electrical characterization of many devices shows an average saturation mobility of 0.12 cm^2/Vs.

To enable real-time characterization of working devices, devices were imaged via KPFM while wired in a transistor device configuration. To facilitate the desired measurements, the device was electrically isolated from the sample chuck of the AFM chamber. A Keithley 2612a power supply was used to output -40 V to the gate electrode, and to provide the -5 V source-drain voltage. A schematic of this wiring scheme is presented in Fig. 1. With the device wired in this configuration, a 40 µm by 40 µm area centered over

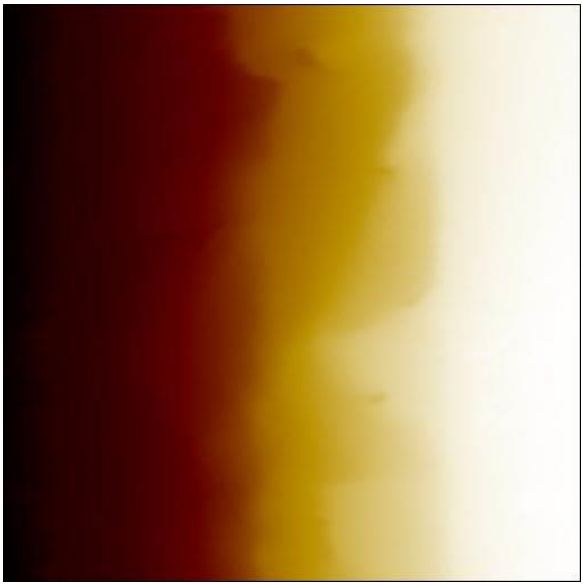

FIG 9. A KPFM potential image of the conduction channel of a diF TESADT thin-film transistor device. This image is 40 µm x 40 µm, the pixel size is 78 nm x 78 nm, and the height range is 4.39 V.

the conduction channel of the device was imaged. An example KPFM potential image of the conduction channel of a diF TESADT thin-film transistor taken in ambient air is shown in Fig. 9, this image is 40 µm x 40 µm, with 512 samples per line and 512 lines. The lightest

areas in Fig. 10 correspond to the highest surface potential, and the darkest areas correspond to the lowest surface potential; the potential range in this example KPFM image is 4.39 ± 0.01V. Much of this work included exposing the same devices to different dopant gases for specific measurements. Prior to all imaging experiments, samples were placed in high vacuum of less than 10^{-6} Torr for at least 720 minutes, as it has been shown absorption of atmospheric dopant gases by organic crystals can be reversed.[41,42]

With this experimental setup, three separate experiments were performed. The goal of the single gas doping experiment was to measure voltage drops along the large grain boundary under a single gas dopant. Prior to imaging, the vacuum chamber was filled with the dopant gas. After the sample had been exposed to the dopant gas for 60 minutes, the sample was moved to the AFM chamber. Multiple sites across multiple 25 µm channel length

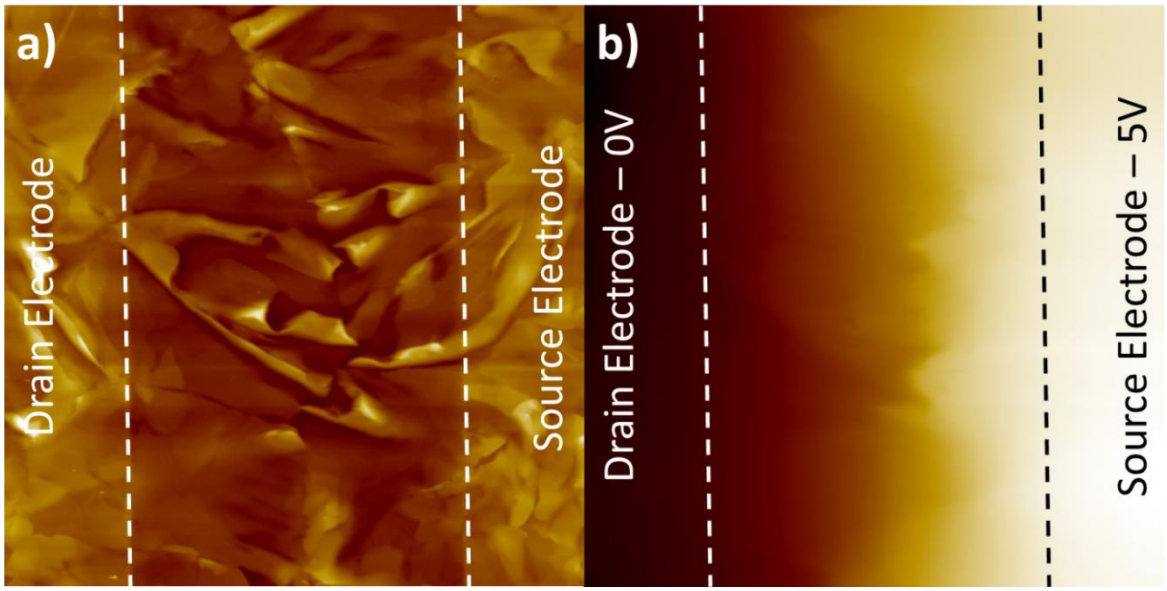

FIG 10. (a) AFM topography and **(b)** KPFM potential images of the conduction channel, 40 µm x 40 µm, 512 pixels per line, 512 lines per image. The source and drain electrodes are highlighted with dotted lines.

devices were imaged and the site location was recorded. The sample was then removed from the AFM chamber to high vacuum, and the dopant exposure process repeated. The same sites

on each device were imaged under each dopant gas,: O_2, N_2, dry air, and ambient air. This process yielded a set of images for each specific site; these images were minimally processed and aligned using Scanned Probe Image Processor (SPIP). All images in this work were processed using a 0^{th} order global flattening algorithm.

An example of the resultant AFM and KPFM images with source and drain electrodes highlighted by dotted lines, shown in the 40 µm x 40 µm images of Figs. 10a and 10b, respectively. To analyze the difference in potential drops across the large grain boundary for

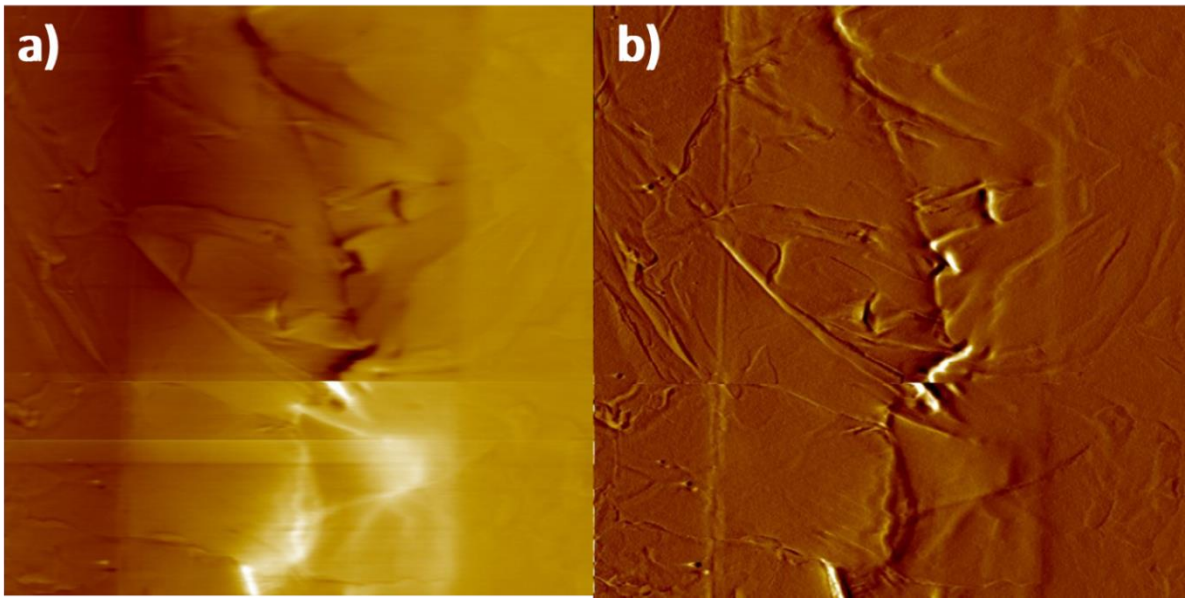

FIG 11. (a) An example of a difference image, here between N2 and O2. **(b)** The horizontal gradient of difference image (a). Brighter pixels correspond to a larger voltage gradient value *dV/dx*. The large grain boundary is visible in the conduction channel of both (a) and (b).

each dopant gas, the aligned potential images were subtracted. Such a resultant difference of electrical potential images is shown in Fig. 11a, where a conduction channel under O_2 image is subtracted from the aligned conduction channel under N_2 image. This subtraction image shows the difference between the image taken in an O_2 environment and the image taken in a N_2 environment and the brightest pixels correspond to the largest difference. The horizontal gradient was calculated for the difference image of Fig. 11a and is shown in Fig. 11b; in this

image many ridges and valleys can be seen, these are regions of greatest horizontal change in the voltage gradient. This figure shows that the degree of change in electric potential drop over the large grain boundary can be quantified. Correspondingly, Fig. 12 outlines the method in which the voltage gradient *dV/dx* was quantified. An individual horizontal line profile was taken from the gradient image, such as Fig. 12, and the maximum magnitude of the voltage gradient relative to the surrounding voltage gradient values at the large grain boundary measured. This measurement was repeated for 10% of the lines for each gradient image and the resulting measurements were averaged. These lines were selected at even

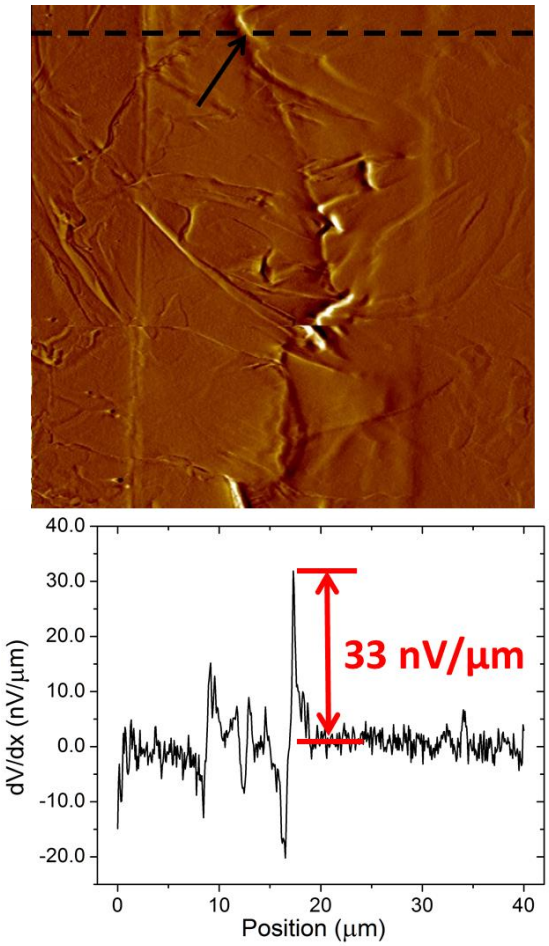

FIG 12. Horizontal gradient of $N_2 - O_2$, as seen in Fig. 11, with an individual line scan shown below for comparison. The dotted line indicates the line scan on the horizontal gradient image, the arrows indicate the voltage gradient peak at the large grain boundary on the image and the line scan. Here the voltage gradient is 33 nV/µm.

intervals across the image. Due to noise in the voltage gradient image overwhelming the voltage gradient measurement on many line profiles, the voltage gradient was quantified for approximately 50 lines. Those average voltage gradient values are given in table I with uncertainties determined by the standard deviation of the mean of the values. Table I gives the mean voltage gradient *dV/dx* and the average fractional change in voltage gradient for the image subtractions between N_2 and O_2, N_2 and ambient air, and N_2 and dry air, and shows that the deviation in the mean of the reported values is of the same order of the mean value itself. This result suggests that the variation of the voltage gradient along the large grain boundary is too great to average over an entire image. This result is not unexpected since pixel sizes are on the order of 80 nm and local grain boundary morphology can vary greatly on much smaller length scales, up to that of the molecule size itself. Such local variance would greatly vary the capacitive charge buildup and, therefore also, the local mobility.

TABLE I. The mean voltage gradient *dV/dx* at the large grain boundary and average fractional change in voltage gradient at the large grain boundary. Values are averaged over measurements from 50 line profile scans.

Specific Subtraction	**Mean Voltage Gradient, dV/dx (mV/μm)**	**Average Fractional Change in voltage gradient, dV/dx (nV/μm)**
$N_2 - O_2$	0.21 ± 0.22	-0.11 ± 0.20
N_2 – Ambient	0.26 ± 0.30	0.08 ± 0.18
N_2 – Dry Air	0.70 ± 0.55	-0.05 ± 0.21

Since the averaging of the voltage gradient *dV/dx* could not be done over an entire image because of the large variations due to morphology, the voltage gradient *dV/dx* was quantified locally. Figure 13a shows a single dopant KPFM potential image, and the horizontal gradient of that potential image is given in Fig. 13b. A line profile was taken at the grain boundary for each image and synchronized to ensure the same line was measured in both images. On the gradient image, there is a peak in the line profile at the large grain boundary. The magnitude and exact position along the line profile of the full-width half max of this peak were found, as indicated in Fig. 13b. This length and position was used as the

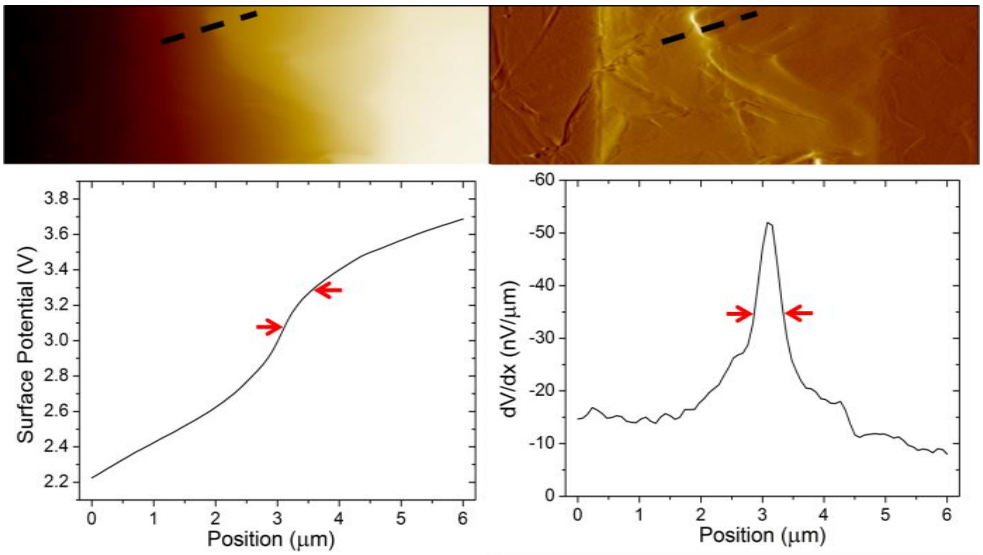

FIG 13. (a) A KPFM potential image with a line profile averaged over a 6-pixel width across the large grain boundary. **(b)** The horizontal gradient of (a) with the corresponding line profile. The FWHM peak indicated by arrows in (b) was used to determine the lateral distance over which to measure the voltage gradient, *dV/dx*, indicated by arrows in (a).

region over which the voltage gradient in the potential image was measured, averaged over 0.5 μm to provide a local determination of the voltage gradient *dV/dx*. This process was repeated for N_2, O_2, dry air, and ambient air. Using this analysis technique, values of the voltage gradient had been measured on the same devices under nitrogen, oxygen, dry air, and ambient air. The fractional change in the voltage gradient from nitrogen to each of the other

gases was found and is given in Table I. As with the previous analysis method, in which the voltage gradient was averaged over the entire image, the variation in the average fractional change was very large.

The time dependent experiments aimed to quantify changes in the voltage gradient at the large grain boundary within the conduction channel. The structure of this device and the interactions between the film and the local environment are complex, thus, a method for quantifying the effects in a meaningful way is needed. For the second experiment, the time-transition experiment, the aim was to observe the evolution of the voltage gradient as the local environment changed from N_2 to a dopant gas, ambient air or dry air. Prior to imaging the conduction channel of the diF TESADT device, the sample was under high vacuum and subsequently the vacuum chamber was filled with N_2. After the device had been exposed to the dopant gas of choice for 60 minutes, the device was transported to the AFM chamber. The device was imaged with KPFM under local N_2 doping for 100 minutes, at which time local doping of N_2 ceased and the AFM chamber was opened to ambient laboratory air. KPFM imaging continued for more than 1000 minutes, capturing over 40 images of the surface while transitioning from N_2 to ambient air at 25 minute intervals. This process was repeated for the transition from N_2 gas to dry air.

The continuous imaging of the conduction channel resulted in a series of images that show the time dependent behavior of the device while transitioning between dopant gases. KPFM images taken were 40 μm by 40 μm, are 512 pixels per line, with 512 lines per image, as seen in the example images in Fig. 11, and were imaged at a 0.7 Hz scan rate, resulting in a 25 minute scan time per image. From a series of such images, changes in the potential image can be seen; specifically, the height value of the surface potential at a given feature

does not remain constant through time. Direct image subtraction analysis, as performed on the data from the first experiment and described above, was performed; however, with the time dependent series of images, voltage gradient measurements were taken at the same position along the large grain boundary on each horizontal gradient image. These voltage gradient values were plotted as a function of time, as seen in Fig. 14. Upon inspection, this analysis method was abandoned, the measurements taken from the gradient of the subtraction

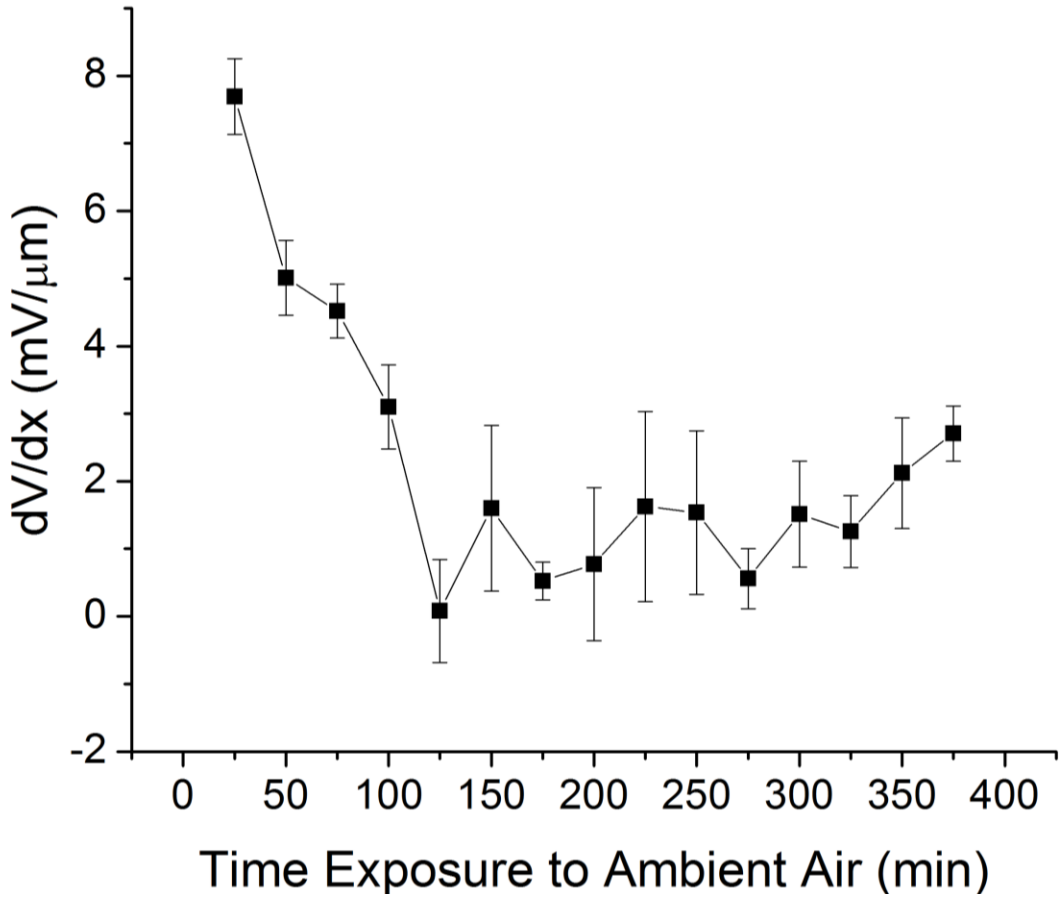

FIG 14. The voltage gradient *dV/dx* as a function of time exposure to ambient air.

images were inconsistent and it was believed that the high amount of image processing required for this analysis method could produce invalid results.

Another analysis method was devised to better understand the evolution of the potential data. All images were aligned, and the same single line profile was plotted from each image in the time series. An example of these line profiles plotted along with the corresponding topographical height profile is given in Fig. 15. In this figure, the potential line profiles are plotted alongside the topographic height line profile so that features in the

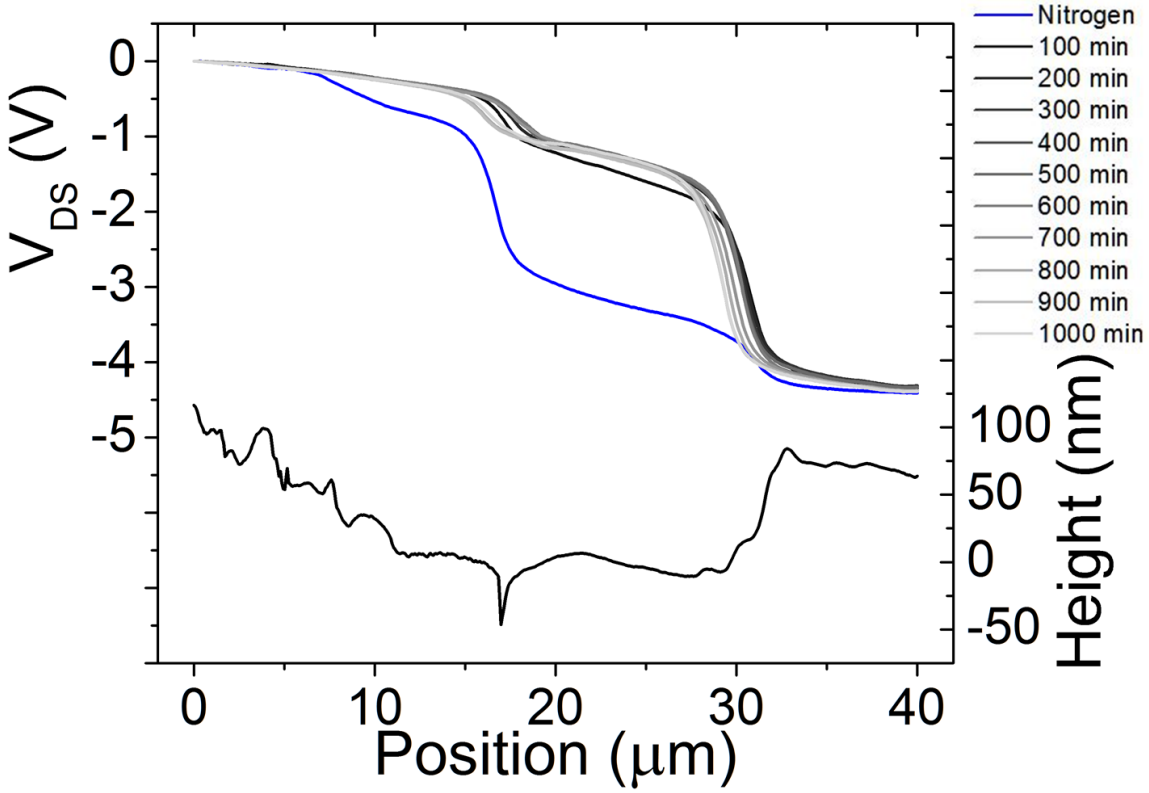

FIG 15. The surface potential and height line profiles of the conduction channel of a diF TESADT TFT under the transition from N_2 to dry air. (top) The surface potential line profiles depict the evolution of drain-source voltage V_{DS} over a 1000 minute transition between dopant gases. (bottom) The height line profile corresponding to the surface potential lines in (top).

surface potential behavior of the device may be related to morphological features in the diF TESADT film. It can be seen that the potential drops in the conduction channel are not static in time with exposure to ambient air, the potential line profiles shift and the slope change from line to line. To quantify the change in the potential drops, the derivative of the potential

line profiles was taken and plotted with the corresponding height line profile, as seen in Fig. 16. The shaded region in Fig. 16 corresponds to the large grain boundary where it can be seen that the magnitude of the voltage gradient peaks at the large grain boundary changes through time. To measure this change in the magnitude of the voltage gradient peaks under ambient air, the peak values of each of the voltage gradient lines at the large grain

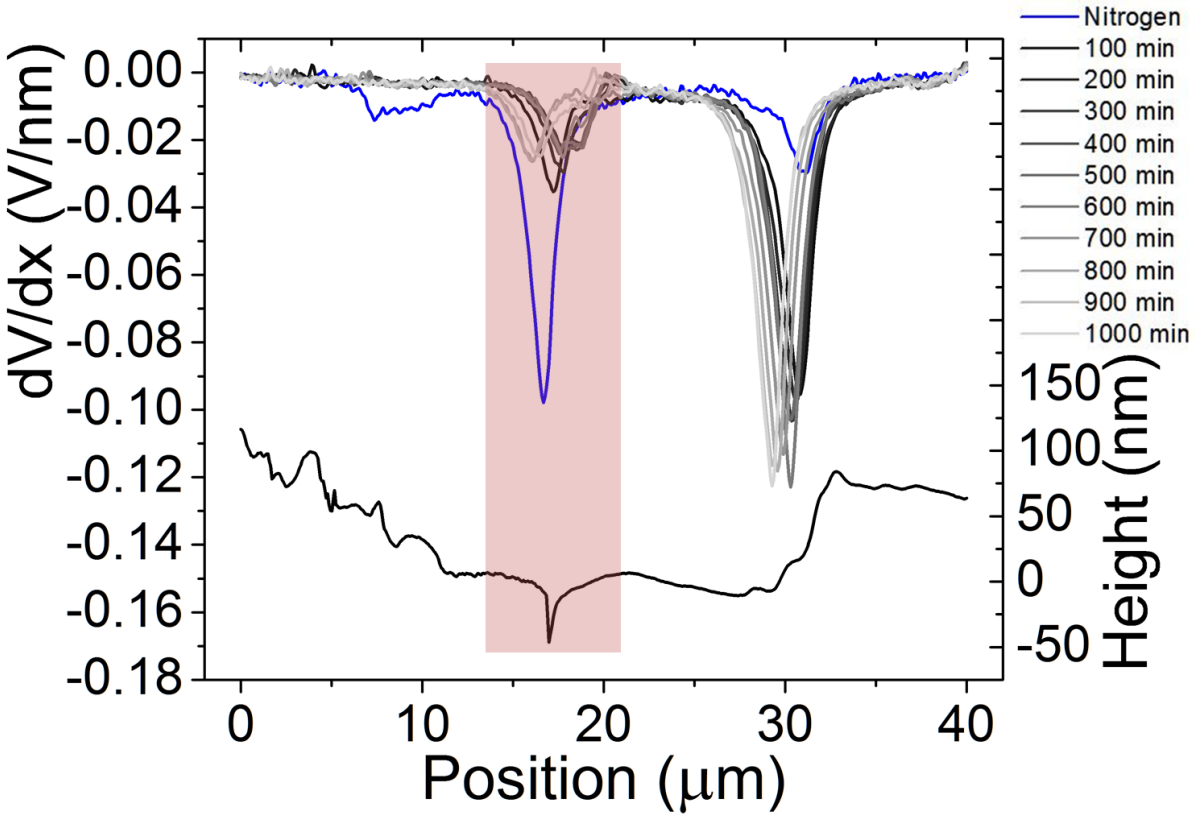

FIG16. The voltage gradient and height line profiles of the conduction channel of a diF TESADT TFT under the transition from N_2 to dry air. (top) The voltage gradient line profiles depict the evolution of the voltage gradient dV/dx over a 1000 minute transition between dopant gases. (bottom) The height line profile corresponding to the voltage gradient lines in (top). The shaded region indicates the large grain boundary region.

boundary were plotted versus time, as seen in Fig. 17. This analysis process was repeated for the time-transition from dry air to ambient air, the peak values at the large grain boundary of the voltage gradient *dV/dx* lines plotted versus time is given in Fig. 18. The peak voltage gradient at the large grain boundary decreases by 57% in the first 300 minutes of imaging for

the transition from N_2 to ambient air, and decreases by 48% in the first 525 minutes of imaging for the transition from dry air to ambient air, see Table II. For both experiments the peak voltage gradient at the large grain boundary plateaus after the initial increase, as seen in Figs. 17 and 18.

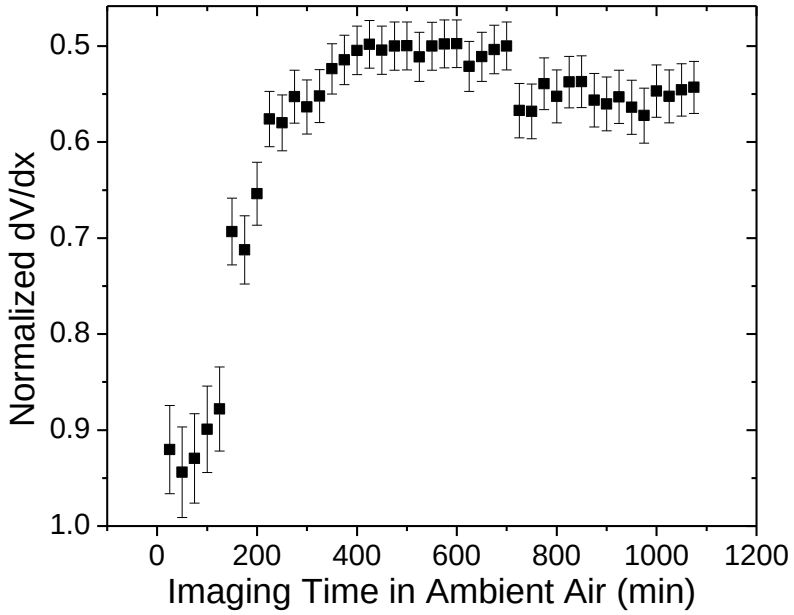

FIG 17. The normalized peak voltage gradient values *dV/dx* as a function of imaging time over the time transition from N_2 to ambient air. Data error bars are the full width half max of the line profile.

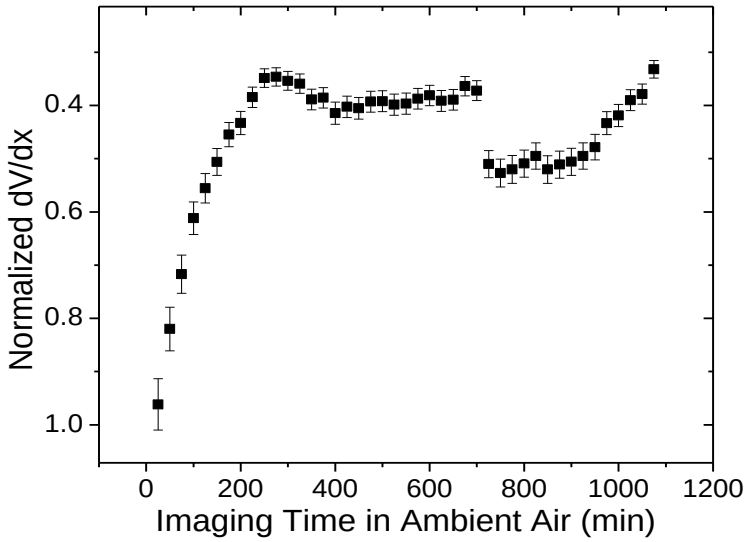

FIG 18. The normalized peak voltage gradient values *dV/dx* as a function of imaging time over the time transition from dry air to ambient air. Data error bars are the full width half max of the line profile.

For the time dependent steady state experiment, devices were imaged as a function of time via KPFM in a steady-state environment, only being exposed to one dopant gas. In one set of experiments, the device was exposed to pure N_2 gas for 60 minutes and moved to the AFM chamber. This device was imaged with KPFM under local N_2 doping for at least 720 minutes and repeated for dry air. The resultant time dependent series of images of the surface potential and topography of the conduction channel under a single gas dopant were analyzed. The line profile analysis, as described above, was performed on this image set. The maximum voltage gradient values at the large grain boundary were plotted versus time under steady-state N_2 doping in Fig. 19 and steady-state dry air doping figure 20. As seen in Fig. 19, the peak voltage gradient at the large grain boundary increases

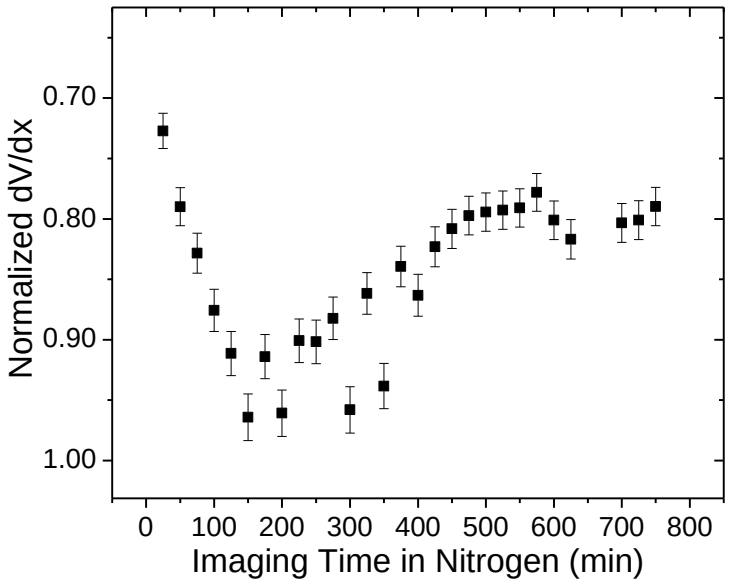

FIG 19. The normalized peak voltage gradient values *dV/dx* as a function of imaging time in N_2 for the time dependent steady state in nitrogen experiment. Data error bars are the full width half max of the line profile.

by 33% in the first 250 minutes of imaging during pure N_2 gas exposure, while the peak voltage gradient at the large grain boundary decreases by 37% in the first 270 minutes of

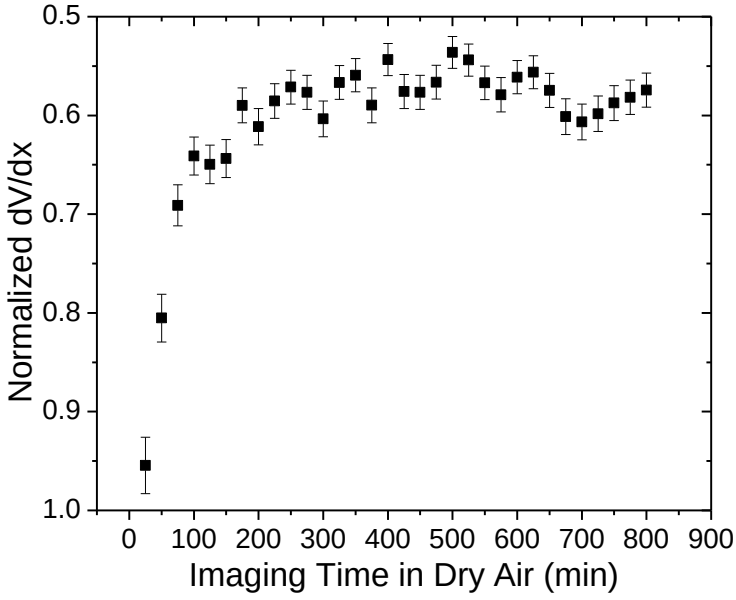

FIG 20. The normalized peak voltage gradient values *dV/dx* as a function of imaging time in dry air for the time dependent steady state in dry air experiment. Data error bars are the full-width half-max of the line profile.

imaging in dry air, as tabulated in Table II. Similarly to the time transition experiment, the peak voltage gradient in dry air remains relatively constant after the initial decrease, as can

be seen in Fig. 20. Additionally, in N_2 the peak voltage gradient is seen to decrease by 15 % over the 250 minutes following the initial increase, as seen in Fig. 19.

TABLE II. The normalized voltage gradient *dV/dx* at the large grain boundary for all time dependent experiments, and the time in minutes of the initial change.

	Grain boundary normalized voltage gradient, dV/dx	**Grain boundary time of initial change (min)**
Steady state N_2	33 ± 3% increase	250
Steady state dry air	37 ± 3% decrease	270
Dry air to ambient air	48 ± 5% decrease	525
N_2 to Ambient Air	57 ± 5% decrease	300

In addition to the evolution of the magnitude of the voltage gradient at the large grain boundary, the horizontal position of the voltage gradient peak was tracked over time. This position was plotted as the horizontal distance from the large grain boundary versus imaging time. A representative plot for the time transition experiment from N_2 to ambient air is given in Fig. 21, where a positive distance indicates movement toward the drain electrode. This figure is exemplary of position versus time plots for all time dependent experiments. The voltage gradient peak shifts away from the large grain boundary toward the drain electrode, shifting a total of approximately 2 μm over 1100 minutes.

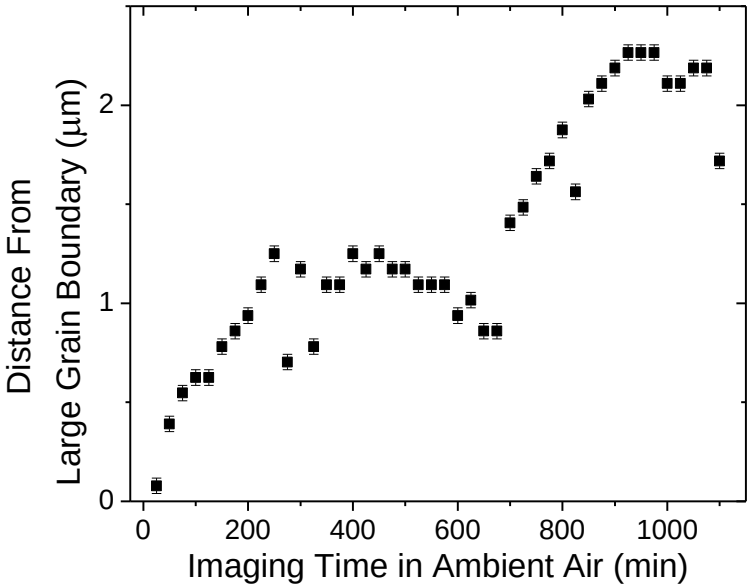

FIG 21. Distance from large grain boundary of voltage gradient *dV/dx* peak position as a function of imaging time in ambient air. Error bars indicate pixel size.

DISCUSSION

The initial line profile scan in N_2, shown in blue in Fig. 15, gives a voltage gradient of 0.5 V/μm across the large grain boundary, which is in agreement with similar measurements by Teague and colleagues[46]. The voltage gradient is proportional to a local resistance to charge transport through the large grain boundary. As shown above in Fig. 20, the measurement of the large grain boundary in pure N_2 gas displays an initial increase in resistance followed by a decrease in resistance, resulting in an overall decrease in the resistance at the large grain boundary of less than 15%. This resistance change in an inert atmosphere of pure N_2 indicates a bias-stress effect, or a change in current-voltage characteristics with the application of voltages over long periods of time. Bias stress can occur due to trapping at the semiconductor dielectric interface or from defects in the semiconductor itself[52].

For comparison, the time dependent steady-state experiment in a dry air environment, shown in Fig. 21, shows the effect of molecular oxygen on the electrical behavior at the grain boundary. In dry air, the local resistance of the large grain boundary initially decreases by 37%. Previous studies by Hu[53] and Hirose[35] have shown that oxygen easily diffuses into grain boundaries. These results are consistent with oxygen intercalation at the large grain boundary. Furthermore, Jurchescu has shown that oxygen, in general, increases local conductivity and positively impacts local electronic transport by attracting generating holes and thereby increasing the number of charge carriers available for conduction[41]. The local measurement in the voltage gradient *dV/dx*, which is proportional to a local measurement of resistance, decreases as the oxygen doping within the diF TESADT film increases, suggesting agreement in both mechanism and measured effect.

The time-transition of the measurement of *dV/dx* at the large grain boundary from a pure N_2 environment to an ambient laboratory air environment shows a relatively large decrease of 57%. The observed *dV/dx* behavior is similar to that of the steady-state measurement of *dV/dx* of the large grain boundary in dry air, even with the additional diffusion of H_2O into the large grain boundary. While it is expected that H_2O will decrease device performance[21,54], it has been shown that oxygen may counteract the negative effects of water in organic devices.[41] Additionally, applying a bias across the device and continuously imaging the same site for long periods of time may cause surface heating. An increase in surface temperature may evaporate some H_2O from the surface and grain boundaries, decreasing any possible effect seen due to H_2O. These results show a resistance decrease that is proportional to the current increase reported by Jurchescu for pentacene single crystal devices exposed to ambient air and light, however the effect reported here takes 6 times longer to occur.

To confirm that the cause is of the resistance decrease of the measurement of local voltage gradient *dV/dx* at the large grain boundary from a pure N_2 environment to an ambient laboratory air environment is due to the inclusion of oxygen in the system and not water, a time-transition measurement of a system from a dry air environment to an ambient air environment is examined, as seen in Fig. 18. The observed trend in voltage gradient is similar to the time-transition from N_2 to ambient air; the resistance decreases initially and then plateaus. The magnitude of the resistance decrease is 57% for the time-transition from N_2 to ambient air, greater than the decrease of 48% for the time-transition from dry air to ambient air. This discrepancy is due to the oxygen doping that occurs prior to imaging for the transition from dry air to ambient air. Thus we see that the addition of H_2O to the local

environment in the presence of oxygen does not significantly impact device behavior at the large grain boundary, the effect of H_2O must be less than a 10% change.

CONCLUSIONS AND FURTHER WORK

We have utilized KPFM to quantify the effects of gas doping at the large grain boundary in diF TESADT TFTs. Over an 800 minute exposure to N_2, local resistance at the large grain boundary increased by 15%. This increase is attributed to bias stress in the device. The steady state in dry air, time transition N_2 to ambient air, and time transition dry air to ambient air all show a decrease in local resistance at the large grain boundary. Thus, O_2 decreases local resistance, O_2 and H_2O decrease local resistance, and slowly adding H_2O in the presence of O_2 decreases local resistance. We conclude that the primary cause of the observed resistance decrease is due to O_2 at the large grain boundary.

While the steady state experiment in dry air shows a decrease in local resistance of 37%, both time transition experiments show a decrease of 50% in local resistance. Thus, when H_2O is present, the decrease in resistance is larger. H_2O is affecting the local electrical performance; however, it is difficult to decouple the effects of H_2O and O_2 from these experiments. To better understand the effect of H_2O, a steady state experiment in ambient air would be helpful. Additionally, it would be useful to take device electrical measurements before and after each experiment so that the results presented here may be put into context of overall device performance changes.

References

[1] J.Y. Lee, K.-T. Lee, S. Seo, and L.J. Guo, Sci. Rep. **4**, (2014).

[2] C.-H. Liu, Y.-C. Chang, T.B. Norris, and Z. Zhong, Nat. Nanotechnol. **advance online publication**, (2014).

[3] Y. Ji, D.F. Zeigler, D.S. Lee, H. Choi, A.K.-Y. Jen, H.C. Ko, and T.-W. Kim, Nat. Commun. **4**, (2013).

[4] A. Pospischil, M.M. Furchi, and T. Mueller, Nat. Nanotechnol. **advance online publication**, (2014).

[5] Y. Yuan, G. Giri, A.L. Ayzner, A.P. Zoombelt, S.C.B. Mannsfeld, J. Chen, D. Nordlund, M.F. Toney, J. Huang, and Z. Bao, Nat. Commun. **5**, (2014).

[6] D.J. Gundlach, Nat. Mater. **6**, 173 (2007).

[7] B.R. Conrad, W.G. Cullen, B.C. Riddick, and E.D. Williams, Surf. Sci. **603**, L27 (2009).

[8] E. Gomar-Nadal, B.R. Conrad, W.G. Cullen, and E.A. Willams, J. Phys. Chem. C **112**, 5646 (2008).

[9] A. Manuelli, A. Knobloch, A. Bernds, and W. Clemens, 2nd Int. IEEE Conf. Polym. Adhes. Microelectron. Photonics POLYTRONIC 2002 Conf. Proc. Cat No02EX599 201 (2002).

[10] Y. Xia, W. Zhang, M.J. Ha, J.H. Cho, M.J. Renn, C.H. Kim, and C.D. Frisbie, Adv. Funct. Mater. **20**, 587 (2010).

[11] A.C. Arias, S.E. Ready, R. Lujan, W.S. Wong, K.E. Paul, A. Salleo, M.L. Chabinyc, R. Apte, R.A. Street, Y. Wu, P. Liu, and B. Ong, Appl. Phys. Lett. **85**, 3304 (2004).

[12] R.A. Street, W.S. Wong, S.E. Ready, I.L. Chabinyc, A.C. Arias, S. Limb, A. Salleo, and R. Lujan, Mater. Today **9**, 32 (2006).

[13] F.C. Krebs, T. Tromholt, and M. Jorgensen, Nanoscale **2**, 873 (2010).

[14] J. Cornil, D. Beljonne, J.-P. Calbert, and J.-L. Brédas, Adv. Mater. **13**, 1053 (2001).

[15] F. Garnier, Chem. Phys. **227**, 253 (1998).

[16] B.R. Conrad, W.G. Cullen, W. Yan, and E.D. Williams, Appl. Phys. Lett. **91**, 242110 (2007).

[17] A.C. Mayer, R. Ruiz, R.L. Headrick, A. Kazimirov, and G.G. Malliaras, Org. Electron. **5**, 257 (2004).

[18] R. Ruiz, A. Papadimitratos, A.C. Mayer, and G.G. Malliaras, Adv. Mater. **17**, 1795 (2005).

[19] R. Ruiz, D. Choudhary, B. Nickel, T. Toccoli, K.C. Chang, A.C. Mayer, P. Clancy, J.M. Blakely, R.L. Headrick, S. Iannotta, and G.G. Malliaras, Chem. Mater. **16**, 4497 (2004).

[20] M.-M. Ling, C. Reese, A.L. Briseno, and Z. Bao, Synth. Met. **157**, 257 (2007).

[21] D.W. Li, E.J. Borkent, R. Nortrup, H. Moon, H. Katz, and Z.N. Bao, Appl. Phys. Lett. **86**, (2005).

[22] R.T. Weitz, K. Amsharov, U. Zschieschang, M. Burghard, M. Jansen, M. Kelsch, B. Rhamati, P.A. van Aken, K. Kern, and H. Klauk, Chem. Mater. **21**, 4949 (2009).

[23] N. Yamazoe, Sens. Actuators B-Chem. **5**, 7 (1991).

[24] J.E. Anthony, Chem. Rev. **106**, 5028 (2006).

[25] K.P. Goetz, Z. Li, J.W. Ward, C. Bougher, J. Rivnay, J. Smith, B.R. Conrad, S.R. Parkin, T.D. Anthopoulos, A. Salleo, J.E. Anthony, and O.D. Jurchescu, Adv. Mater. **23**, 3698 (2011).

[26] S.S. Lee, C.S. Kim, E.D. Gomez, B. Purushothaman, M.F. Toney, C. Wang, A. Hexemer, J.E. Anthony, and Y.-L. Loo, Adv. Mater. **21**, 3605 (2009).

[27] T. Sekitani, U. Zschieschang, H. Klauk, and T. Someya, Nat. Mater. **9**, 1015 (2010).

[28] T. Sekitani, T. Yokota, U. Zschieschang, H. Klauk, S. Bauer, K. Takeuchi, M. Takamiya, T. Sakurai, and T. Someya, Science **326**, 1516 (2009).

[29] E.C.P.M., Simon G. J.van Hal, Paul A.Setayesh, SepasGeuns, Thomas C. T.Mutsaers, Kees A. H. A. Cantatore, Eugenio Wondergem, Harry J. Werzer, Oliver Resel, Roland Kemerink, Martijn Kirchmeyer, Stephan Muzafarov, Aziz M. Ponomarenko, Sergei A.de Boer, BertBlom, Paul W. M.de Leeuw, Dago M. Smits, Nature **455**, 956 (2008).

[30] S.K. Park, D.A. Mourey, S. Subramanian, J.E. Anthony, and T.N. Jackson, Appl. Phys. Lett. **93**, (2008).

[31] D.J. Gundlach, J.E. Royer, S.K. Park, S. Subramanian, O.D. Jurchescu, B.H. Hamadani, A.J. Moad, R.J. Kline, L.C. Teague, O. Kirillov, C.A. Richter, J.G. Kushmerick, L.J. Richter, S.R. Parkin, T.N. Jackson, and J.E. Anthony, Nat. Mater. **7**, 216 (2008).

[32] R.J. Kline, S.D. Hudson, X.R. Zhang, D.J. Gundlach, A.J. Moad, O.D. Jurchescu, T.N. Jackson, S. Subramanian, J.E. Anthony, M.F. Toney, and L.J. Richter, Chem. Mater. **23**, 1194 (2011).

[33] J.W. Ward, M.A. Loth, R.J. Kline, M. Coll, C. Ocal, J.E. Anthony, and O.D. Jurchescu, J. Mater. Chem. **22**, 19047 (2012).

[34] S.M. Huston, J.Y. Wang, M.A. Loth, J.E. Anthony, B.R. Conrad, and D.B. Dougherty, J. Phys. Chem. C **116**, 21465 (2012).

[35] M. Hirose, E. Tsunemi, K. Kobayashi, and H. Yamada, Appl. Phys. Lett. **103**, 173109 (2013).

[36] J. Rivnay, L.H. Jimison, J.E. Northrup, M.F. Toney, R. Noriega, S. Lu, T.J. Marks, A. Facchetti, and A. Salleo, Nat. Mater. **8**, 952 (2009).

[37] T. Someya, H.E. Katz, A. Gelperin, A.J. Lovinger, and A. Dodabalapur, Appl. Phys. Lett. **81**, 3079 (2002).

[38] T.W. Kelley and C.D. Frisbie, J. Phys. Chem. B **105**, 4538 (2001).

[39] J. Chen, C.K. Tee, M. Shtein, J. Anthony, and D.C. Martin, J. Appl. Phys. **103**, (2008).

[40] M.C. Tanese, D. Fine, A. Dodabalapur, and L. Torsi, Biosens. Bioelectron. **21**, 782 (2005).

[41] O.D. Jurchescu, J. Baas, and T.T.M. Palstra, Appl. Phys. Lett. **87**, (2005).

[42] R.B. Ye, M. Baba, K. Suzuki, Y. Ohishi, and K. Mori, Thin Solid Films **464**, 437 (2004).

[43] K.-J. Lee, K. Ihm, T.-H. Kang, and S. Chung, Surf. Sci. **603**, 3445 (2009).

[44] Z.T. Zhu, J.T. Mason, R. Dieckmann, and G.G. Malliaras, Appl. Phys. Lett. **81**, 4643 (2002).

[45] D.H. Dunlap, P.E. Parris, and V.M. Kenkre, Phys. Rev. Lett. **77**, 542 (1996).

[46] L.C. Teague, B.H. Hamadani, O.D. Jurchescu, S. Subramanian, J.E. Anthony, T.N. Jackson, C.A. Richter, D.J. Gundlach, and J.G. Kushmerick, Adv. Mater. **20**, 4513 (2008).

[47] U. Zaghloul, B. Bhushan, F. Coccetti, P. Pons, and R. Plana, J. Vac. Sci. Technol. A **29**, (2011).

[48] K.C. Dickey, J.E. Anthony, and Y.-L. Loo, Adv. Mater. **18**, 1721 (2006).

[49] M.M. Payne, S.A. Odom, S.R. Parkin, and J.E. Anthony, Org. Lett. **6**, 3325 (2004).

[50] M.M. Payne, S.R. Parkin, J.E. Anthony, C.C. Kuo, and T.N. Jackson, J. Am. Chem. Soc. **127**, 4986 (2005).

[51] S. Subramanian, S.K. Park, S.R. Parkin, V. Podzorov, T.N. Jackson, and J.E. Anthony, J. Am. Chem. Soc. **130**, 2706 (2008).

[52] D. Knipp, R.A. Street, A. Volkel, and J. Ho, J. Appl. Phys. **93**, 347 (2003).

[53] Y. Hu, G.F. Dong, Y.C. Hu, L.D. Wang, and Y. Qiu, J. Phys. -Appl. Phys. **39**, 4553 (2006).

[54] Y. Qiu, Y.C. Hu, G.F. Dong, L.D. Wang, J.F. Xie, and Y.N. Ma, Appl. Phys. Lett. **83**, 1644 (2003).

Vita

Cortney Anne Hughes Bougher was born in Statesville, North Carolina to Frank Hughes and Julie Villeneuve. She graduated from Avery County High School in June 2001. She attended Caldwell Community College and Technical Institute and was awarded the Associate in Arts degree in May 2008. The following spring, she entered Appalachian State University to study Physics, and in May 2012 she earned the Bachelor of Science degree in Applied Physics and Applied Mathematics. In the fall of 2012, Ms. Bougher accepted a research assistantship at Appalachian State University and began study toward a Master of Science degree in Engineering Physics. The M.S. was awarded in May 2014. Ms. Bougher accepted a position with the American Physical Society in May 2014, where she continues to work in the membership division.

Ms. Bougher is a member of Sigma Pi Sigma. She resides in Maryland with her son.